

Improving Position Sensor Accuracy Through Spatial Harmonic Decoupling, and Sensor Scaling, Offset, and Orthogonality Correction Using Self-Commissioning MRAS Methods

Caleb W. Secrest, Jon S. Pointer, Michael R. Buehner, *Member, IEEE*, and Robert D. Lorenz, *Life Fellow, IEEE*

Abstract—This paper presents methods for improving the accuracy of vector-based position measurements through the decoupling of multiple nonideal sensor properties using model reference adaptive system (MRAS) techniques. The nonideal sensor properties considered are: signal scaling errors (amplitude imbalance on the vector components), signal offsets, imperfect orthogonality (quadrature error) between sensor vector components, and additional spatial harmonics superimposed on fundamental sensor outputs. Simulation and experimental results are provided to evaluate the proposed MRAS-based decoupling methods. The methods presented here can be applied to multiple forms of vector-based position measurement and estimation such as the use of magnetoresistive sensors, sine/cosine encoders, resolvers, or self-sensing (sensorless) methods. These methods can be implemented in real time and are well-suited to the self-commissioning of vector-based position sensors for enhanced sensor accuracy.

Index Terms—AC motor drives, magnetoresistive position sensor, model reference adaptive system (MRAS), position measurement, resolver, self-sensing (sensorless) control, sensor harmonics, sine/cosine encoders.

NOMENCLATURE

θ_{rm}	Rotor mechanical position.
$\omega_{\text{rm}}, \Omega_{\text{rm}}$	Rotor mechanical velocity.
θ_e	Ideal sensor vector phase angle.
θ_{err}	Observer estimated position error.
J_p	Rotor physical inertia.
b_o, k_{so}, k_{iso}	Motion observer controller gains.
K_1, K_2	Model reference adaptive system (MRAS) adaptive controller gains.

Manuscript received February 9, 2015; revised May 7, 2015; accepted May 8, 2015. Date of publication June 10, 2015; date of current version November 18, 2015. Paper 2015-IDC-0065.R1, presented at the 2014 IEEE Energy Conversion Congress and Exposition, Pittsburgh, PA, USA, September 20–24, and approved for publication in the IEEE TRANSACTIONS ON INDUSTRY APPLICATIONS by the Industrial Drives Committee of the IEEE Industry Applications Society. This work was supported by Woodward, Inc., Fort Collins, CO, USA.

C. W. Secrest and R. D. Lorenz are with the Wisconsin Electric Machines and Power Electronics Consortium (WEMPEC), University of Wisconsin–Madison, Madison, WI 53706 USA (e-mail: secrest@wisc.edu; lorenz@engr.wisc.edu).

J. S. Pointer and M. R. Buehner are with Woodward, Inc., Fort Collins, CO 80525 USA (e-mail: Jon.Pointer@Woodward.com; Michael.Buehner@Woodward.com).

Color versions of one or more of the figures in this paper are available online at <http://ieeexplore.ieee.org>.

Digital Object Identifier 10.1109/TIA.2015.2443100

X	Real component of sensor output vector.
Y	Imaginary component of sensor output vector.
\bar{Z}	Sensor output vector.
A_x, A_y	Sensor signal offset terms.
h	Spatial harmonic number.
h_{err}	Fund. component of position measurement error.
B_{xh}, B_{yh}	Magnitude of the h th sensor harmonic.
ϕ_{xh}, ϕ_{yh}	Phase of the h th sensor harmonic.
T	Sample period.
j	Complex number $\sqrt{-1}$.
(\wedge)	Estimated physical parameter.

I. INTRODUCTION

IDEALLY, vector-based position sensors output two orthogonal signals, one of which correlates to the sine of the sensor angle, and another of which correlates to the cosine of the sensor angle. Together, these signals create a rotating vector that has a phase correlating to the angular position of the machine shaft. Position sensors that output a rotating vector, such as sine/cosine encoders, resolvers, and magnetoresistive position sensors, are widely used in machine motion control applications. In back electromotive force (EMF) and spatial saliency tracking, the machine magnetic properties are utilized such that the machine becomes a vector-based position sensor [1]. In [2], it was shown that even the discrete nature of Hall effect-based position measurement and incremental optical encoders can be interpreted as rotating vectors containing significant spatial harmonic content. In practice, vector-based position sensor outputs may contain scaling errors (amplitude imbalance), orthogonality (quadrature) errors, signal offset errors, and additional spatial harmonics. These errors can be the result of the sensor structure itself (e.g., discrete position information when using Hall effect-based position measurement or incremental optical encoders), realistic manufacturing limitations for symmetry (e.g., inductance harmonics in a resolver or machine resulting from tooth/slotting effects and discrete windings), or may occur during signal conditioning and sampling (e.g., amplifier and/or analog-to-digital offset and scaling errors). Furthermore, these errors may drift over time with temperature or age, and when unaccounted for, these nonideal sensor properties produce spatially dependent measurement errors [3].

Multiple methods exist to reduce sensor-induced measurement errors. Some methods rely on least squares fitting of an ellipse to the image traced by the sensor output vector as it rotates [4]–[6]. Another method decomposes the sensor vector into positive sequence and negative sequence components to extract a vector with essentially no offset, amplitude, and orthogonality errors [7]. In [8], the d -axis current of a permanent-magnet synchronous motor (PMSM) is used to extract sensor amplitude, and orthogonality information. In [9], trigonometric analysis-based methods are presented to adaptively suppress the effects of offset, amplitude, and orthogonality errors. While the methods in [4]–[9] result in improved sensor accuracy, these methods neglect sensor additional spatial harmonics making them ill-suited for sensors with significant harmonic content, or for spatial saliency tracking-based self-sensing when multiple spatial saliencies exist in an ac machine [1]. In [10], interpolation and lookup tables are used to correct the reference model for a phase-locked loop (PLL), but the sources of the errors were not directly identified and the PLL has inherent lag properties.

Properly formed vector tracking Luenberger-style observers provide zero-lag filtering of velocity and position estimates and have been shown to be a reduced noise alternative to arc-tangent calculations and a zero-lag alternative to vector tracking state filters (PLLs) [11]. Previous work presented a decoupling form of vector tracking a Luenberger-style observer for improved self-sensing based rotor position estimation when multiple spatial saliencies exist in an ac machine [1]. Multiple spatial saliencies in an ac machine are analogous to the presence of additional spatial harmonics in an external position sensor's output. In [1], it was shown that the decoupling of all but one of the multiple spatial saliencies resulted in improved rotor position estimation accuracy and estimation dynamics. [12] utilized the decoupling technique presented in [1] to improve position estimation accuracy when using extremely low-resolution Hall effect position sensing. In [1] and [12], harmonic decoupling was not adaptive such that variations in sensor properties during operation were not considered.

In this paper, a magnetoresistive position sensor is investigated and MRAS-based methods are developed and presented to adaptively estimate and decouple sensor signal offsets, scaling and orthogonality errors, and additional spatial harmonic components. The nonideal sensor properties are decoupled from the sensor output vector using the decoupling form of vector tracking observer presented in [1]. The final result of the MRAS-based decoupling is improved rotor position measurement/estimation accuracy. The methods presented here can be applied to many forms of vector-based position measurement such as the use of magnetoresistive sensors, sine/cosine encoders, resolvers or self-sensing (sensorless) methods. These methods can be implemented in real time and are well-suited to the self-commissioning of vector-based position sensors for enhanced sensor accuracy. Development of the MRAS structure is presented along with simulation and experimental evaluation.

II. MODELING NONIDEAL SENSOR PROPERTIES AND THE RESULTING POSITION ESTIMATION ERRORS

The magnetoresistive position sensor investigated here produces two signals that together form a vector rotating at twice

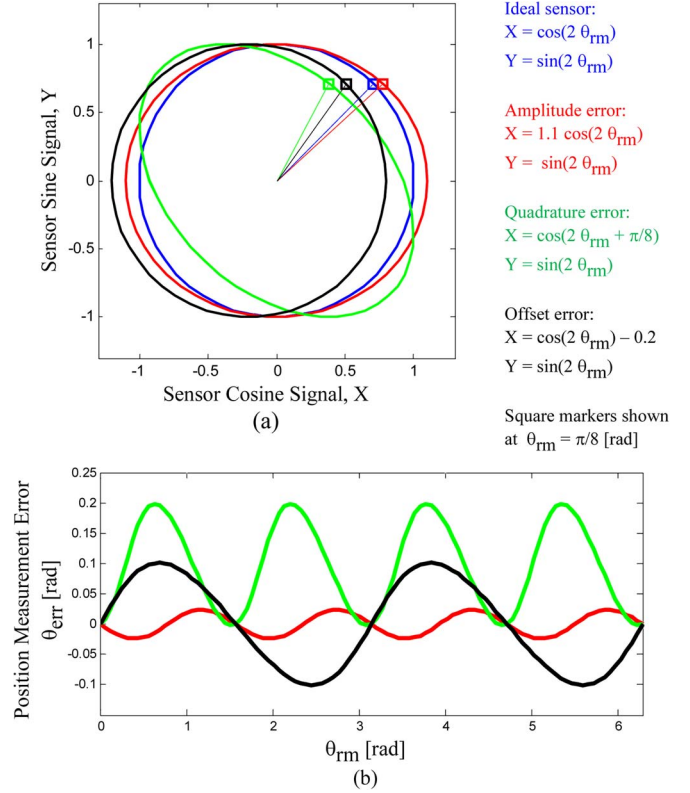


Fig. 1. (a) Sensor vector image plot displaying image shape deviation from an ideal sensor for various nonideal sensor properties. (b) Resulting position measurement error due to nonideal sensor properties.

the mechanical shaft speed. Considering the nonideal properties discussed in the previous section, the sensor outputs can be modeled, as shown in (1)–(3). Here, the fundamental components of the sensor signals have been separated from the spatial Fourier series summation terms. This is to distinguish the sensor's fundamental components from any additional (undesirable) sensor spatial harmonics. In addition, note that the fundamental sine signal in (2) contains no phase shift term. A phase shift term is omitted here to provide an absolute reference for the sensor output vector with respect to the machine rotor angle, and also provide an absolute reference for the orthogonality of the two sensor fundamental outputs, which is now solely determined by ϕ_{x1}

$$X = A_x + B_{x1} \cos(2\theta_{rm} + \phi_{x1}) + \sum_{h=2}^{\infty} B_{xh} \cos(2h\theta_{rm} + \phi_{xh}) \quad (1)$$

$$Y = A_y + B_{y1} \sin(2\theta_{rm}) + \sum_{h=2}^{\infty} B_{yh} \sin(2h\theta_{rm} + \phi_{yh}) \quad (2)$$

$$\bar{Z} = X + jY. \quad (3)$$

Fig. 1(a) displays examples of the images traced by the sensor output vector when scaling, offset, or orthogonality errors exist in the sensor. Fig. 1(b) shows the resulting position measurement errors due to these nonideal sensor properties. Here, the position measurement error, θ_{err} , is defined as the angle between the ideal sensor vector and the nonideal sensor vector as a function of rotor position. From Fig. 1, it is clear that

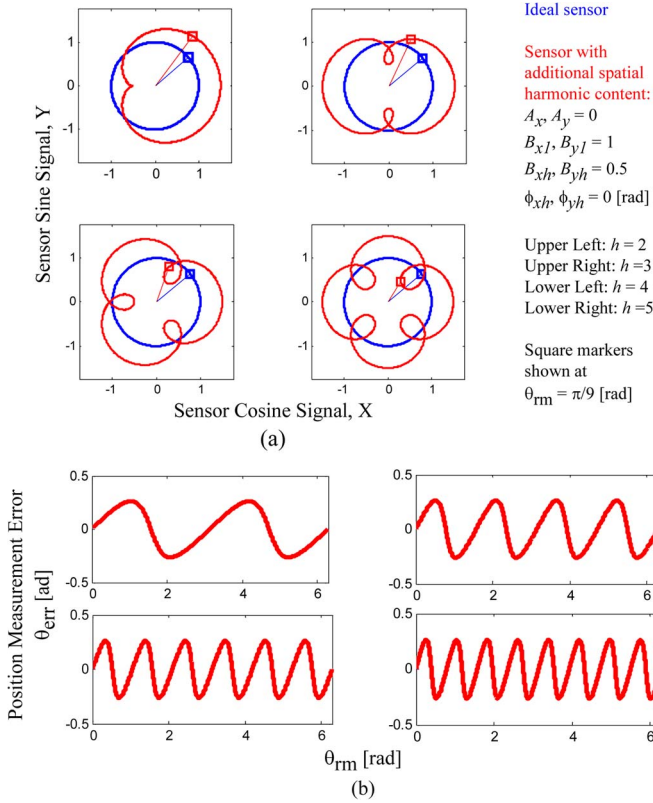


Fig. 2. (a) Sensor vector image plot displaying image shape for various additional sensor spatial harmonics. (b) Resulting position measurement error due to additional sensor spatial harmonics.

for the sensor under investigation, signal offset errors primarily produce a second spatial harmonic position measurement error. Furthermore, signal scaling and orthogonality errors both primarily produce fourth spatial harmonic position measurement errors. In [3], the mathematics behind the position measurement errors resulting from nonideal sensor properties is covered.

Fig. 2(a) displays examples of the images traced by the sensor output vector when additional spatial harmonics are present in the sensor outputs. Fig. 2(b) shows the resulting position measurement errors due to these nonideal sensor properties. From Fig. 2, it can be inferred that the fundamental component of the position measurement error, h_{err} , due to the h th sensor spatial harmonic component will follow (4). Again, the mathematics behind the position measurement errors induced by additional sensor spatial harmonic components is covered in [3]

$$h_{err} = 2(h - 1). \quad (4)$$

Table I summarizes the sensor properties discussed here and the fundamental spatial harmonic component of each properties' resulting systematic position measurement error.

III. DEVELOPMENT OF MRAS-BASED NONIDEAL SENSOR PROPERTY ESTIMATION AND DECOUPLING

A general MRAS structure is presented in [13], and shown here in Fig. 3. In an MRAS structure, the "reference model" represents a desirable actual process behavior. The MRAS structure calculates the error between the output of the actual

TABLE I
NONIDEAL SENSOR PROPERTIES AND FUNDAMENTAL SPATIAL HARMONIC COMPONENTS OF THE RESULTING SYSTEMATIC POSITION MEASUREMENT ERRORS

Sensor Property	Sensor Signal Harmonic	Resulting Spatial Harmonic Measurement Error
Offset Errors	-	2 nd
Amplitude Imbalance	1	4 th
Imperfect Quadrature	-	4 th
Additional Harmonics	h	2(h - 1)

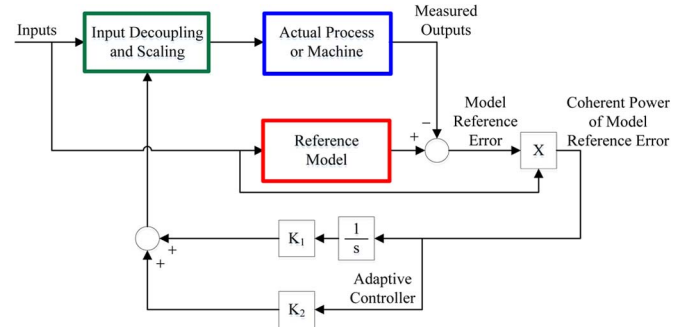


Fig. 3. General MRAS block diagram [13].

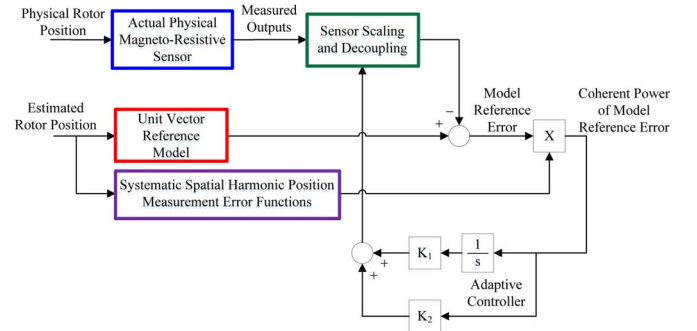


Fig. 4. Nonideal sensor property scaling and decoupling MRAS system level block diagram.

physical process and the output of the reference model. The resulting "Model Reference Error" (MRE) is then multiplied by an input (or function of inputs) to the actual process. The purpose of this multiplication is to extract the components of the MRE, which are coherent with specific known actual process inputs. The resulting "Coherent Power of MRE" (CPMRE) is then delivered to an adaptive controller with a proportional and integral term. The output of the adaptive controller is then used to manipulate the scaling of a process parameter estimate or decouple a process term that contributes to the CPMRE. The goal of the MRAS structure is to drive the actual process behavior to match that of the reference model such that the CPMRE is driven to zero.

A. MRAS-Based Nonideal Sensor Property Decoupling Conceptual Block Diagram

Fig. 4 displays a reformulation of Fig. 3 into a diagram that is specific to nonideal sensor property decoupling. The

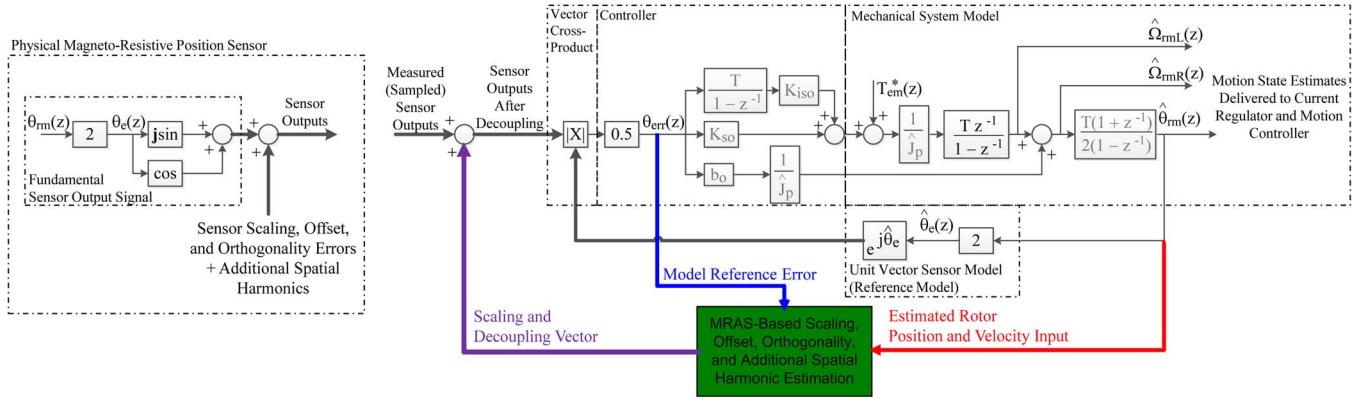


Fig. 5. (Left) Model of physical position sensor. (Right) Decoupling form of Luenberger-style vector tracking motion observer, including placement of the MRAS-based nonideal sensor property estimation and decoupling structure and its input/output signals. MRAS components shown in color.

physical magnetoresistive position sensor represents the “actual process.” Note that decoupling of nonideal properties takes place on the measured outputs of the sensor rather than on the inputs to the actual process. Referring back to (1) and (2), for the sensor under investigation, it is desired that the sensor outputs produce a unit vector rotating at twice mechanical speed (i.e., $A_x = A_y = 0$; $B_{xh} = B_{yh} = 0$ for $h > 1$; $\phi_{x1} = 0$; and $B_{x1} = B_{y1} = 1$). This ideal sensor model will be used as the reference model to which the physical sensor outputs (after decoupling) will be compared. The MRE will then be calculated as the difference in phase between the unit vector reference model and the physical measured sensor outputs after decoupling. Referring to Table I, it is known that each nonideal sensor property produces a predictable and systematic spatial harmonic position measurement error. By correlating the MRE with these known spatial harmonic position measurement error functions, the MRE coherent with each specific nonideal sensor property can be extracted. The resulting CPMRE signals will be sent to adaptive controllers whose outputs will decouple each nonideal sensor property contributing to the MRE. This process is shown in Fig. 4.

B. Decoupling Form of Vector Tracking Observer

The decoupling form of Luenberger-style vector tracking motion observer presented in [1] and utilized here is shown in Fig. 5. The inputs to the motion observer are the sensor’s measured outputs, and the output of the observer, i.e., $\hat{\theta}_{rm}$, is the position feedback signal delivered to the current regulator and motion controller. Also shown in Fig. 5, is the placement of the MRAS structure with respect to the vector tracking motion observer. Fig. 5 reveals some of the key MRAS structural components and signals. On the left side of Fig. 5 is a model of the physical position sensor. The input to the sensor is the physical rotor shaft position, and the “sensor outputs” are the two signals produced by the sensor, which together form the vector being tracked by the observer. The “sensor outputs” contain the superposition of both the “fundamental sensor output signals” and the “sensor scaling, offset, orthogonality, and additional spatial harmonic” components. The goal of the MRAS structure is to estimate a “scaling and decoupling vector” both equal and opposite to the “sensor scaling, offset, orthogonality, and

additional spatial harmonic” vector such that when the scaling and decoupling vector is summed with the measured sensor outputs only the fundamental (ideal) sensor output components remain.

The MRAS structure’s unit vector reference model already exists as part of the motion observer structure and is labeled in Fig. 5. The input to the reference model is the estimated rotor shaft position, and the output is a unit vector that rotates at twice the mechanical speed. The MRE can be extracted from the vector tracking observer’s vector cross-product. The output of the vector cross-product is proportional to the sine of the angle between the sensor output vector after decoupling and the unit vector sensor model. Given that the unit vector sensor model is tracking the sensor output vector, the angle between the two vectors will be sufficiently small such that small angle assumption applies and the output of the vector cross-product can be treated as approximately equal to the angle between the two vectors.

The remaining portions of the MRAS structure: calculation of the coherent power of MRE, the adaptive controllers, and the formulation of the sensor scaling and decoupling vector are shown in Fig. 6 and will be discussed in the following sections.

C. MRAS-Based Signal Offset Correction and Sensor Second Harmonic Decoupling

Referring to Figs. 1, 2, and Table I, the harmonic functions needed to calculate the CPMRE within the MRAS structure are known. Offset errors, and the sensor’s second harmonic ($h = 2$), produce position measurement errors that correlate to a second spatial harmonic of the machine’s rotor position. Therefore, MREs that correlate with a second spatial harmonic rotating unit vector (i.e., correlate with $e^{j2\hat{\theta}_{rm}}$) can be reduced by decoupling the sensor offset terms (i.e., the sensor A_x and A_y terms) and by decoupling the sensor second harmonic terms associated with B_{x2} , B_{y2} , ϕ_{x2} , and ϕ_{y2} . Practically, it is not necessary to include decoupling terms for both offset errors and the sensor’s second harmonic component. By manipulating only the sensor signal offset terms the position measurement errors induced by the sensor’s second harmonic will also be decoupled. That is, the net measurement error contribution from

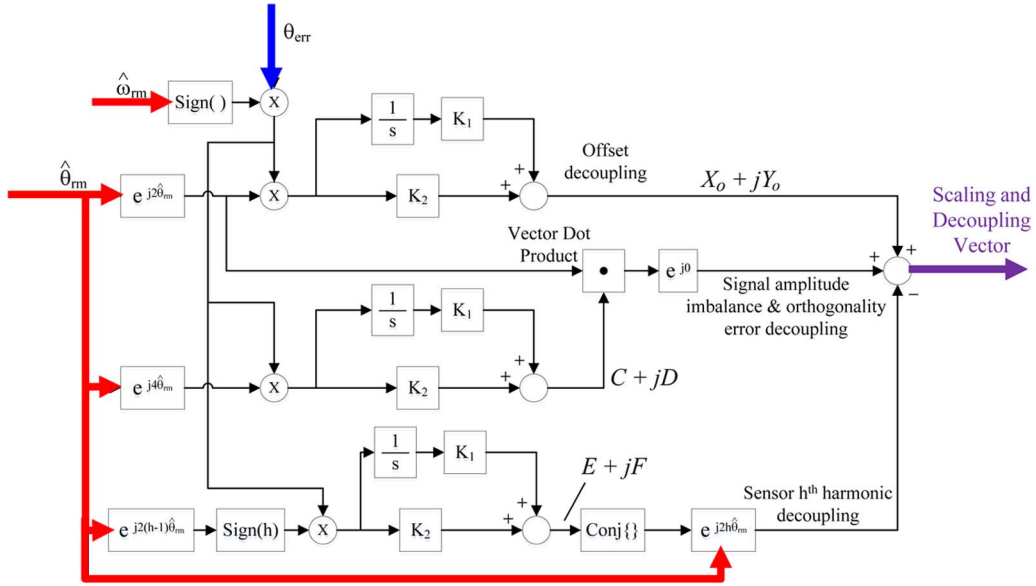


Fig. 6. Detailed MRAS structure for estimation of sensor signal offset, amplitude, and orthogonality errors and h th spatial harmonic decoupling.

both offset errors and the sensor's second harmonic will be decoupled by correlating the MRE with $e^{j2\hat{\theta}_{rm}}$ and using the result to manipulating only the signal offset terms.

Fig. 6 shows the MRAS formulation of the signal offset decoupling vector. As described earlier, the MRE is correlated to a second spatial harmonic rotating unit vector, $e^{j2\hat{\theta}_{rm}}$, and the resulting CPMRE is passed through an adaptive controller with gains K_1 and K_2 . The result is an offset decoupling vector, $(X_o + jY_o)$, which will correctly decouple both signal offset errors and the sensor's second spatial harmonic. As an aside, note that for the coherent power of MRE to accumulate consistently within the adaptive controllers, the direction of the machine's rotation must be taken into account. This is shown in Fig. 6 by multiplication of the MRE with the sign of the estimated rotor velocity.

To better understand how the signal offset decoupling vector, i.e., $(X_o + jY_o)$, can simultaneously decouple both signal offset errors and the sensor's second harmonic component, consider a sensor containing only these two nonideal properties. Note that after proper decoupling, the imaginary component of the sensor output, Y , divided by the real component of the sensor output, X , must equal the tangent of the angle being measured. This statement can be expressed mathematically, as shown in (5). The X_o and Y_o terms in (5) represent the signal offset decoupling vector components that are output from the MRAS structure. Given that (5) must be true for all angles (i.e., $0 \leq \theta_{rm} < 2\pi$) and angle can be selected and substituted into (5) to solve for the relationship between X_o , Y_o , A_x , A_y , B_2 , and ϕ_2 . These relationships are shown in (6) and (7)

$$\tan(2\theta_{rm}) = \frac{A_y + \sin(2\theta_{rm}) + B_2 \sin(4\theta_{rm} + \phi_2) + Y_o}{A_x + \cos(2\theta_{rm}) + B_2 \cos(4\theta_{rm} + \phi_2) + X_o} \quad (5)$$

$$Y_o = -A_y - B_2 \sin(\phi_2) \quad (6)$$

$$X_o = -A_x + B_2 \cos(\phi_2). \quad (7)$$

Equations (6) and (7) represent the closed-form solutions for the signal offset decoupling vector components that will simultaneously decouple both signal offset errors and the sensor's second harmonic component. Note that these closed-form solutions are provided only for completeness, and that the MRAS structure automatically converges upon the correct X_o and Y_o vector components without the need for experimental effort or knowledge of A_x , A_y , B_2 , and ϕ_2 .

Fig. 7 displays examples of the sensor offset decoupling vector correcting sensor offsets [see Fig. 7(a)] and decoupling sensor second harmonic terms [see Fig. 7(b)]. Note that Fig. 7 displays nonideal sensor properties being decoupled independently for clarity, but in practice all sensor errors discussed in this paper can exist simultaneously and will still be successfully decoupled through the MRAS. The MRAS does, however, assume that sensor harmonics occur equally in both magnitude and phase on both the sine (Y) and cosine (X) signals (i.e., $B_{xh} = B_{yh}$ and $\phi_{xh} = \phi_{yh}$ for $h > 1$). In Fig. 7, the magenta vector represents the MRAS-based decoupling vector. When the decoupling vector is added to the measured sensor outputs (red), the decoupled sensor outputs produce a phase relationship exactly equal to the ideal sensor (blue). Note that only the phase of the decoupled sensor output vector is used to determine the rotor angular position, but differences in magnitude between the reference model vector (blue) and the sensor outputs after decoupling (red + magenta) will contribute to the gain and thus bandwidth (BW) of the observer. In the Fig. 7 legend, the equations for the measured sensor outputs are shown in black text. The decoupling vector equations are shown as magenta text summed onto the sensor outputs.

D. MRAS-Based Amplitude & Orthogonality Error Correction and Sensor Third Harmonic Decoupling

Sensor signal amplitude imbalance, orthogonality errors, and the sensor's third harmonic ($h = 3$) all produce fourth spatial

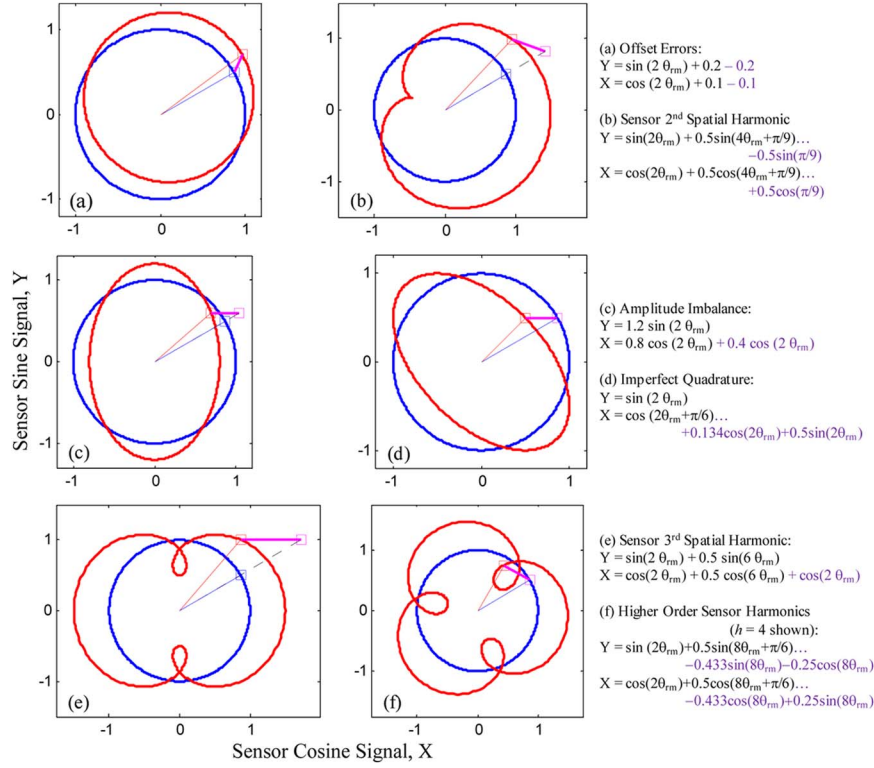


Fig. 7. Sensor error decoupling vector (magenta), when added to the measured sensor outputs (red), produces the ideal sensor phase relationship (blue/dotted-black).

harmonic position measurement errors. Similar to the case for offset and sensor second harmonic decoupling, it is not necessary to independently consider all three sources of error to minimize their net contribution to a fourth spatial harmonic position measurement error through decoupling. Here, only the fundamental scaling and orthogonality errors need to be directly considered in the MRAS. Furthermore, it is not necessary to alter the scaling of both the sine and cosine sensor signals to achieve the desired decoupling. By altering only the cosine signal scaling, B_{x1} , until it matches that of the sine signal scaling, B_{y1} , the desired decoupling will be achieved. Although the resulting sensor signal vector will have a magnitude equal to B_{y1} , and not unity, the correct sensor phase relationship will still be attained. In addition, by only manipulating the cosine signal, a degree of freedom is removed from the MRAS leaving only a single solution for the MRAS system to converge upon (i.e., B_{x1} must converge upon B_{y1}). To decouple orthogonality errors, recall that the phase of the sine signal has been defined as equal to zero in (2), such that only the phase of the cosine signal, ϕ_{x1} , requires decoupling.

Two trigonometric identities relevant to the simultaneously decoupling of both amplitude imbalance and imperfect quadrature errors are shown in (8) and (9). In (8), the leftmost term represents the real component (X -signal) of the measured output from the physical sensor, as shown in (1), the term added to the sensor output (the middle term) represents the decoupling term, and the term on the right of the equality represents the desired sensor output after decoupling. Note that the desired sensor output after decoupling has amplitude B_{y1} and phase $\phi_{dcp1} = 0$ (i.e., amplitude equal to that of the sine signal and

phase equal to zero). From (8), it is shown that for a given B_{x1} , B_{y1} , and ϕ_{x1} , with $\phi_{dcp1} = 0$, there exists a solution for R and β that will correctly and simultaneously decouple both the sensor signal amplitude imbalance and orthogonality errors

$$B_{x1} \cos(2\theta_{rm} + \phi_{x1}) + R \cos(2\theta_{rm} - \beta) = B_{y1} \cos(2\theta_{rm} - \phi_{dcp1}) \quad (8)$$

$$\text{where } B_{y1}^2 = B_{x1}^2 + R^2 + 2B_{x1}R \cos(-\phi_{x1} - \beta)$$

$$\tan \phi_{dcp1} = \left(\frac{R \sin \beta - B_{x1} \sin \phi_{x1}}{R \cos \beta + B_{x1} \cos \phi_{x1}} \right)$$

$$R \cos(2\theta_{rm} - \beta) = C \cos(2\theta_{rm}) + D \sin(2\theta_{rm}) = (C + jD) \cdot e^{j2\theta_{rm}} \quad (9)$$

$$\text{where } R^2 = C^2 + D^2 \text{ and } \tan \beta = D/C$$

$$C = B_{y1} (1 - \cos(\phi_{x1})) + (B_{y1} - B_{x1}) \cos(\phi_{x1}) \quad (10)$$

$$D = B_{x1} \sin(\phi_{x1}). \quad (11)$$

The identity displayed in (9) is used for implementation purposes. Shown in Fig. 6, by correlating the MRE to a fourth spatial harmonic rotating unit vector, $e^{j4\hat{\theta}_{rm}}$, the CPMRE for scaling and orthogonality errors is calculated. Note that the CPMRE is a vector quantity. The CPMRE is then passed through an adaptive controller with gains K_1 and K_2 . The result is a vector that has the necessary C and D coefficients (as shown in (9)) to properly decouple signal scaling (amplitude) and orthogonality (quadrature) errors. A vector dot product

between the vector output from the adaptive controller, $(C + jD)$, and a second spatial harmonic rotating vector, $e^{j2\hat{\theta}_{\text{rm}}}$, is performed next, and the resulting scalar becomes the magnitude of a vector lying solely along the real axis. (10) and (11) display the closed-form solutions for the C and D vector coefficients, which will simultaneously decouple both signal scaling and orthogonality errors. Note again that the MRAS structure does not directly solve (8)–(10), or (11) but automatically converges upon the correct C and D coefficients without the need for experimental effort or prior knowledge of B_{x1} , B_{y1} , or ϕ_{x1} .

The sensor's third harmonic ($h = 3$) also contributes to fourth spatial harmonic position measurement errors. Similar to the offset decoupling vector's capability to also decouple the sensor's second harmonic ($h = 2$), the amplitude imbalance and orthogonality error decoupling vector will automatically decouple the sensor's third spatial harmonic with no need for additional MRAS structural components. It should be noted that for $\phi_{x3} = \phi_{y3} \neq 0$, there will be a small, but constant, residual position measurement error (i.e., $\theta_{\text{rm}} - \hat{\theta}_{\text{rm}} = \phi_{\text{err}} = \text{constant}$) induced by the MRAS-based decoupling. This is due to the indirect nature of the sensor third harmonic decoupling. As mentioned, this error is small but will depend on the magnitude and phase of the third harmonic. This is an acceptable tradeoff considering the improvements made to smooth torque production and motion observer dynamics.

To better understand how the amplitude imbalance and orthogonality error decoupling vector will also decouple the sensor's third spatial harmonic component, consider a sensor containing only a third harmonic nonideal property. Recall that after proper decoupling, the imaginary component of the sensor output, Y , divided by the real component of the sensor output, X , must equal the tangent of the angle being measured. This statement can be expressed mathematically, as shown in (12), at the bottom of the page. The terms in (12) with coefficients C and D represent the signal amplitude imbalance and orthogonality error decoupling vector components, corresponding to (9), that are output from the MRAS structure. Note that the ϕ_{err} term induced by the indirect nature of the third harmonic decoupling is also considered in (12). Given that (12) must be true for all angles (i.e., $0 \leq \theta_{\text{rm}} < 2\pi$) and angle can be selected and substituted into (12) to solve for the relationships between C , D , ϕ_{err} , B_3 , and ϕ_3 . Equation (13), at the bottom of the page, shows a relationship that can be derived by substituting $\theta_{\text{rm}} = -\phi_{\text{err}}$ into (12). The expression in (13) can be used to determine the residual error term, ϕ_{err} , given the magnitude and phase of the sensor's third spatial harmonic component, B_3 and ϕ_3 , respectively. After calculating ϕ_{err} , it can be shown that

the closed-form solutions for the C and D decoupling vector coefficients, which will correctly decouple the sensor's third spatial harmonic component, can be expressed as shown in (14) and (15), at the bottom of the page. Again, (12)–(15) are shown only for completeness, and knowledge of B_3 and ϕ_3 is not required for the MRAS structure to perform properly.

Fig. 7 displays examples of the MRAS-based decoupling vector correctly decoupling amplitude imbalance errors [see Fig. 7(c)], signal orthogonality errors [see Fig. 7(d)], and sensor third harmonic components [see Fig. 7(e)].

E. MRAS-Based Higher Order Sensor Harmonic Decoupling

Shown in Table I, the magnetoresistive position sensor's higher order harmonics ($h > 3$) produce systematic spatial harmonic position measurement errors according to (4). Equations (16) and (17) display trigonometric identities relevant to the decoupling of higher order sensor harmonics. Equation (18) displays the decoupling terms from (16) and (17) in a vector format. Again, it should be noted that these identities are displayed only for clarity. The MRAS structure does not directly solve the equations, but automatically converges upon the correct E and F coefficients with no need for experimental effort or prior knowledge of B_{xh} , B_{yh} , ϕ_{xh} , or ϕ_{yh} .

In (16)–(18), the terms on the right side of the equality represent the h th harmonic component of the physical sensor, as shown in (1) and (2). The terms on the left side of the equality represent scalar, i.e., (16), (17), and vector, i.e., (18), forms of the decoupling vector that will be estimated by the MRAS. For completeness, the closed-form solutions for the E and F higher order harmonic decoupling vector coefficients are shown in (19) and (20)

$$E \cos(2h\theta_{\text{rm}}) + F \sin(2h\theta_{\text{rm}}) = B_{xh} \cos(2h\theta_{\text{rm}} - \phi_{xh}) \quad (16)$$

$$E \sin(2h\theta_{\text{rm}}) - F \cos(2h\theta_{\text{rm}}) = B_{yh} \sin(2h\theta_{\text{rm}} - \phi_{yh}) \quad (17)$$

$$(E - jF)e^{j2h\theta_{\text{rm}}} = B_{xh} \cos(2h\theta_{\text{rm}} - \phi_{xh}) + jB_{yh} \sin(2h\theta_{\text{rm}} - \phi_{yh}) \quad (18)$$

where $B_{xh}^2 = B_{yh}^2 = E^2 + F^2$ and $\tan \phi_{xh} = \tan \phi_{yh} = F/E$

$$E = \sqrt{\frac{B_{xh}^2}{1 + \tan^2(\phi_{xh})}} \quad (19)$$

$$F = -\sqrt{B_{xh}^2 - E^2}. \quad (20)$$

$$\tan(2(\theta_{\text{rm}} + \phi_{\text{err}})) = \frac{\sin(2\theta_{\text{rm}}) + B_3 \sin(6\theta_{\text{rm}} + \phi_3)}{\cos(2\theta_{\text{rm}}) + B_3 \cos(6\theta_{\text{rm}} + \phi_3) + C \cos(2(\theta_{\text{rm}} + \phi_{\text{err}})) + D \sin(2(\theta_{\text{rm}} + \phi_{\text{err}}))} \quad (12)$$

$$0 = \sin(-2\phi_{\text{err}}) + B_3 \sin(-6\phi_{\text{err}} + \phi_3) \quad (13)$$

$$C = 2B_3 \cos(-6\phi_{\text{err}} + \phi_3) \quad (14)$$

$$D = -2B_3 \sin(-6\phi_{\text{err}} + \phi_3) \quad (15)$$

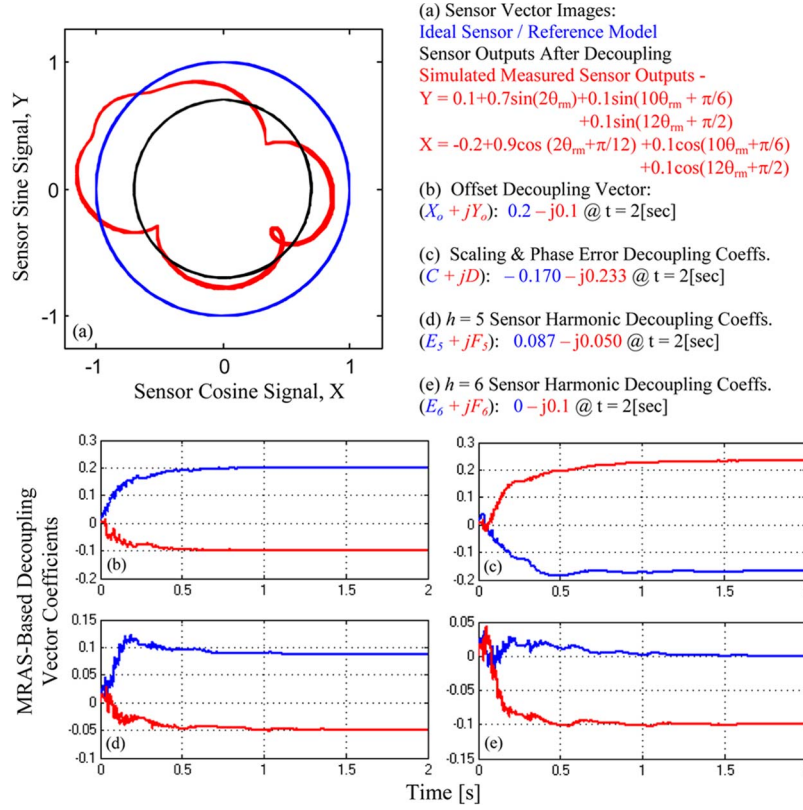


Fig. 8. Simulation-based example of MRAS-based nonideal sensor property decoupling showing. (a) Sensor vector images before and after decoupling. (b)–(e) MRAS convergence on decoupling vector coefficients.

Shown in Fig. 6, by correlating the MRE to the spatial harmonic rotating unit vector $e^{j2(h-1)\hat{\theta}_{rm}}$ the CPMRE for the h th sensor harmonic is calculated. Note that the CPMRE is a vector quantity. The CPMRE is then passed through an adaptive controller with gains K_1 and K_2 . The result is a vector, $(E + jF)$, which has the necessary E and F coefficients [as shown in (16)–(20)] to properly decouple the h th sensor signal harmonic. Following (18), the complex conjugate of the vector output from the adaptive controller is then modulated via a sensor h th spatial harmonic rotating unit vector, $e^{j2h\hat{\theta}_{rm}}$. It should be noted that the MRAS structure can correctly decouple both positively rotating higher order harmonics ($h > 0$) and negatively rotating higher order harmonics ($h < 0$) requiring only that the sign (polarity) of h be considered within the correlation function, as shown in Fig. 6 with the block labeled “sign(h).” The mathematics of (16)–(20) do not depend on the sign of h .

As shown in Fig. 6, the final MRAS-based sensor nonideal property decoupling vector consists of the summation of the signal offset decoupling vector (which incorporates sensor second spatial harmonic decoupling), the amplitude imbalance & orthogonality error decoupling vector (which incorporates sensor third spatial harmonic decoupling), and any number of h th spatial harmonic decoupling vectors for $h > 3$ or $h < 0$. Note that each sensor harmonic with $h > 3$ requires a unique rotating correlation vector, $e^{j2(h-1)\hat{\theta}_{rm}}$, adaptive controller, and rotating modulation vector, $e^{j2h\hat{\theta}_{rm}}$. This means that each significant additional harmonic with $h > 3$ will require its own signal path within the MRAS structure.

IV. EVALUATION OF THE MRAS-BASED NONIDEAL SENSOR PROPERTY DECOUPLING TECHNIQUES

The vector tracking motion observer, and MRAS structure for nonideal sensor property decoupling, as shown in Figs. 5 and 6, respectively, have been implemented both experimentally and in simulation. The following section will display key experimental and simulation results.

A. Simulation-Based Evaluation of MRAS-Based Nonideal Sensor Property Decoupling Techniques

In simulation, a sensor with extreme offset, scaling, orthogonality, and spatial harmonic distortion was considered. For the simulation shown, the motion observer EVs were tuned to 100, 10, and 1 Hz, the adaptive controller gains were $K_1 = 50$ and $K_2 = 0.1$, and the machine’s motion profile was a 1 Hz, 100 rad/s sine trajectory. The simulation results are displayed in Fig. 8. From Fig. 8(a), it is shown that even in the presence of significant sensor distortion, the MRAS converges upon and decouples the nonideal sensor properties. The sensor outputs after decoupling (black) have an identical phase relationship, as a function of shaft position, to the ideal sensor reference model (blue). This is seen here by the fact that the sensor outputs after decoupling and the reference model outputs form concentric circles. Note that the sensor outputs after decoupling (black) are signals internal to the motion observer and MRAS structure and are not directly utilized for machine control purposes. Instead, these signals are provided as an input to the motion observer’s

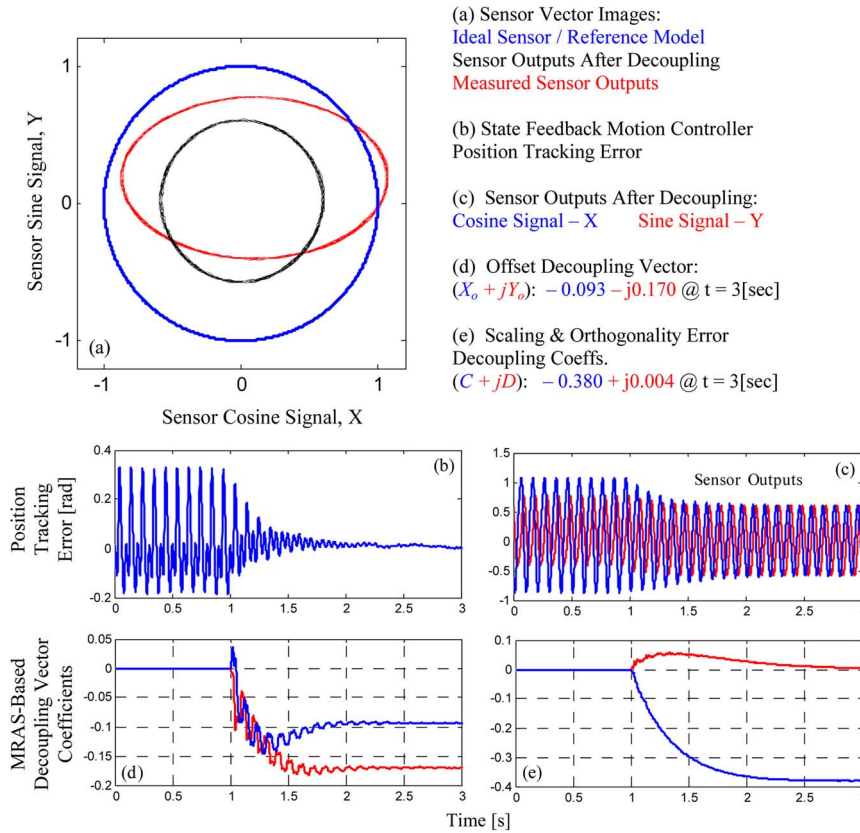


Fig. 9. Experimental example of MRAS-based nonideal sensor property decoupling showing. (a) Sensor vector images before and after decoupling. (b) Position loop command tracking error. (c) Sensor sine and cosine output signals. (d)–(e) MRAS convergence on decoupling vector coefficients. Adaptive controller gains: $K_1 = 85$ and $K_2 = 0.1$.

vector cross product, replacing the measured sensor outputs (red), and resulting in improved motion observer dynamic properties and motion state estimation accuracy.

B. Experimental-Based Evaluation of MRAS-Based Nonideal Sensor Property Decoupling Techniques

The sensor used for experimental evaluation of the proposed methods is an NXP Semiconductors magnetic field sensor, model KMZ41. The sensor was utilized to determine the rotor position of an ElectroCraft RP34-112V48 SPMSM. For the experimental results shown, the motion observer EVs were tuned to 200, 20, and 2 Hz, and the machine was operated at a 5 [rev/s] constant speed under low bandwidth (5 Hz) motion control. If higher bandwidth was used, then the machine would track the nonideal sensor properties, and the estimated velocity would appear constant while the physical velocity oscillated. Low bandwidth motion control was used here such that the physical shaft velocity is relatively constant and the sensor-induced position and velocity errors appear in the motion state estimates. This was done solely for demonstration purposes in this paper and, in practice, the motion controller can be fully tuned to meet an application's bandwidth requirements without a reduction in MRAS performance. MRAS was turned on after 1 [s] of data collection. Results are shown in Figs. 9 and 10.

In the experimental example displayed in Fig. 9, the amplitude of the sine (Y) signal was reduced to approximately 66% of its nominal value, and offset errors inherent in the sensor

outputs were unaccounted for prior to activation of the MRAS-based decoupling. This was done intentionally to induce errors that would be clearly visible in the polar sensor image shown in Fig. 9(a) and in the sensor time-domain output signals shown in Fig. 9(c). From Fig. 9(a), the sensor image prior to decoupling (red) forms an elliptical shape that is not centered about zero. After the MRAS is activated, the sensor image after decoupling (black) is circular and centered about zero. Again, the sensor image after decoupling and the reference model outputs form concentric circles. As mentioned, given the low bandwidth motion control utilized here, sensor-induced position measurement errors will present themselves within the position loop command tracking error. This is displayed in Fig. 9(b). From Fig. 9(b), for the results shown, after approximately 1[s] the sensor-induced position errors have been significantly reduced. The sensor sine and cosine output signals are shown versus time in Fig. 9(c). In Fig. 9(c), it is clear that, prior to MRAS activation, the sine and cosine signals are not equal in amplitude and are not center about zero, and that after MRAS is activated the amplitude imbalance and offset errors are significantly reduced. Fig. 9(d) and (e) display the convergence of the MRAS decoupling vector coefficients.

For the experimental results displayed in Fig. 10, the sensor signal amplitudes and offsets were initially calibrated by noting the maximum and minimum values of each sensor signal over multiple rotations and applying scaling and offset corrections in software to reduce offset errors and amplitude imbalance. However, this type of offline calibration is subject to signal noise, additional sensor harmonic content, and does not

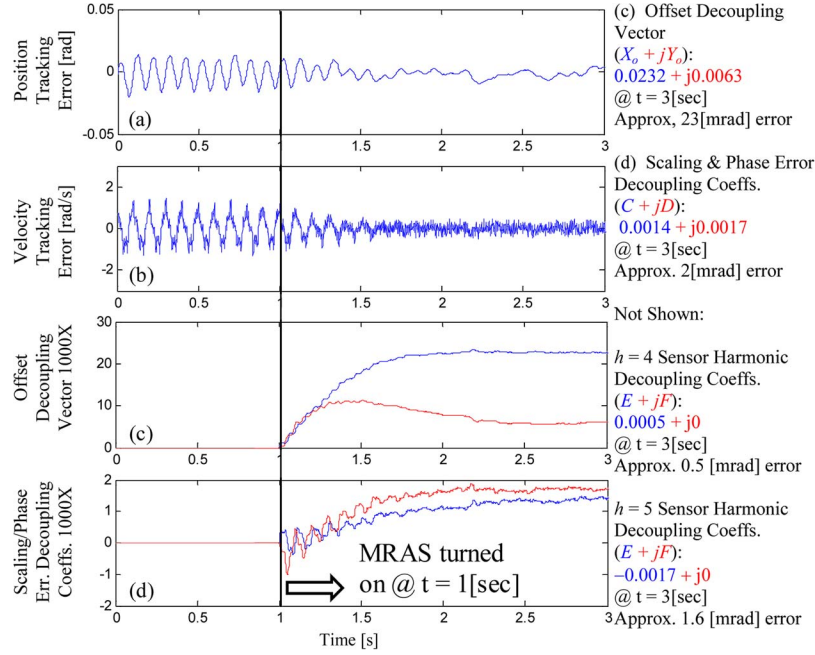


Fig. 10. Experimental example of MRAS-based nonideal sensor property decoupling showing. (a) and (b) Position and velocity command tracking error signals. (c) and (d) MRAS convergence on decoupling vector coefficients. Adaptive controller gains: $K_1 = 35$ and $K_2 = 0.05$.

consider variations during operation. As a result, after offline calibration, sensor nonideal properties remain. From Fig. 10(a) and (b), before MRAS is activated, large second spatial harmonic oscillating position and velocity command tracking errors exist. This implies that offset errors and sensor second harmonic terms are dominant nonideal properties that remain in the position sensor even after offline calibration. Upon activation, the MRAS begins to converge on estimates for the sensor's nonideal components. For the results shown, after approximately 1 [s] the sensor-induced errors, which appear in the position loop command tracking error signal have been significantly reduced from approximately 34 [mrad]_{pk-pk} (~ 2 [deg]) to less than 7 [mrad]_{pk-pk} (~ 0.4 [deg]). The residual position command tracking errors likely result from the low BW motion control used, and additional sensor harmonics that have not been included in the MRAS. If the system was driving a significant inertial load in order to achieve a more constant physical velocity, or if a high accuracy sensor were included in the test fixture and the accuracy of the magnetoresistive sensor was directly calculated, it is expected that the documented improvements would be even greater.

Fig. 10(c) and (d) display the MRAS convergence on the offset decoupling vector and the amplitude imbalance and orthogonality error decoupling vector coefficients. In addition, included in the experiment was the estimation of the $h = 4$ and $h = 5$ sensor harmonic decoupling vector coefficients. The estimated coefficients are displayed in the legend of Fig. 10.

V. PRACTICAL IMPLEMENTATION CONCERNS

A. MRAS Sensitivity to Estimated Physical Inertia

The motion observer displayed in Fig. 5 requires an estimate of the physical inertia of the machine and driven load, \hat{J}_p .

The most significant role of the estimated inertia in the motion observer is to accurately scale the feedforward torque input, T_{em}^* , in order to provide a near zero-lag estimate of the machine motion states beyond the bandwidth of the motion observer. Given that the \hat{J}_p value utilized within the observer is selected by the control engineer, and the observer gains, b_o , K_{so} , and K_{iso} , are calculated with absolute knowledge of this estimate, the value of \hat{J}_p plays no significant role in the observer's motion state estimation accuracy within the observer bandwidth. Since the MRAS structure fundamentally operates within the bandwidth of the observer (i.e., depends on the observer's error signal), the MRAS structure is inherently insensitive to \hat{J}_p estimation errors. This parameter insensitivity is displayed in Fig. 11, which will be discussed further in the next section.

B. MRAS Sensitivity to Disturbance Torque

If the motion observer shown in Fig. 5 contained a perfect open-loop model of the physical system from T_{em}^* to $\hat{\theta}_{rm}$, then closed-loop feedback control of the observer structure would not be necessary in order to obtain accurate motion state estimates. The observer feedback controller is, however, a practical necessity required to compensate for imperfect system modeling and unknown disturbances that act on the system. The fundamental operation of the MRAS structure developed here relies on this observer feedback characteristic to extract unmodeled position sensor properties that appear in the feedback error signal of the observer structure. One consequence of utilizing the observer feedback error signal is that torque disturbances acting on the machine contribute to this signal and are therefore included in the MRE input to the MRAS structure. Recall, however, that the MRE is not the signal delivered to

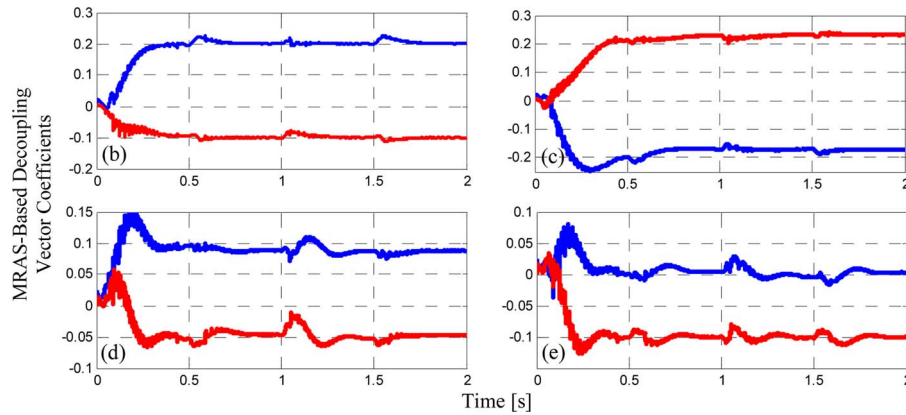


Fig. 11. Simulation-based example showing MRAS convergence on decoupling vector coefficients, whereas under a 0.5 [p.u.] friction torque load and using estimated inertia of 0.66 J_p in motion observer. See Fig. 8 for simulated sensor nonideal properties and motion trajectory.

MRAS adaptive controllers. Instead, the MRE is correlated to spatially harmonic rotating unit vector functions to calculate the CPMRE, and this CPMRE signal is then delivered to the adaptive controllers. The result is that torque disturbances that do not correlate spatially with the rotating unit vector functions do not, on average, contribute to the sensor error decoupling vector.

To demonstrate the MRAS structure insensitivity to non-spatial torque disturbances, and incorrect inertia estimates, Fig. 11 displays a simulation result using the same nonideal sensor properties, MRAS structure tuning, and 1 Hz, 100 [rad/s] sine wave motion trajectory that was used to generate Fig. 8, but now the simulation has been modified to include a significant friction torque load and J_p estimation error. Note that at the velocity zero crossing the simulated friction torque load quickly changes polarity creating a highly dynamic step change in torque loading conditions. From Fig. 11, it is observed that these nonspatial, highly dynamic, step torque changes cause perturbations in the MRAS-based decoupling vector coefficients at 0.5, 1.0, and 1.5 [s] (where the 1-Hz velocity trajectory crosses zero), but that these perturbations are relatively small and are corrected within the MRAS structure quickly. It should be stated that the magnitude of the perturbations directly depends on the K_1 and K_2 gains in the MRAS adaptive controllers. By reducing these gains the sensitivity to nonspatial disturbances can be further reduced at the expense of slower decoupling vector coefficient convergence dynamics. By comparing the final decoupling vector coefficients converged upon by the MRAS in Figs. 8 and 11, it is shown that the J_p estimation error produces no significant deterioration in the MRAS structure's capability to converge on the correct decoupling vector coefficients.

In the case that a spatial harmonic torque disturbance *does* correlate spatially with one of the rotating unit vector functions in the MRAS structure, the MRAS structure will interpret the torque disturbance as a sensor error and will manipulate the sensor until the CPMRE associated with the given spatial harmonic is driven to zero. This is not a desired outcome, and at the point that the CPMRE is driven to zero, the motion controller stiffness to this spatial harmonic will be solely defined by the

physical inertia of the system. This will be discussed further in the next section.

C. MRAS Sensitivity to Current Sensor Scaling and Offset Errors

Current sensor scaling and offset errors induce spatially harmonic torque pulsations in machine drives due to the fact that during current regulation these erroneous feedback signals are driven to track the current reference. Current sensor scaling errors induce a spatially harmonic pulsating torque with a harmonic number corresponding to the pole count of the machine, whereas current sensor offset errors induce torque pulsations with harmonic number corresponding to the number of the machine pole pairs. Similar to the discussion in the previous section, if current sensor-induced torque pulsations correlate with the rotating unit vector functions in the MRAS structure, then the structure will interpret the torque disturbance as a position sensor error and will manipulate the position sensor decoupling vector until the CPMRE associated with these harmonics is driven to zero. Again, under this condition, the motion controller disturbance rejection stiffness to these spatial harmonics will be solely defined by the physical inertia of the system.

If possible, the MRAS structure should not be operated under conditions, in which the MRAS correlation functions, share spatial harmonic numbers with known spatially harmonic disturbance torques. However, when considering the effects of spatially harmonic disturbance torques on the MRAS structure discussed here, it is important to draw a significant distinction between the dynamic characteristics of spatial torque disturbances and position sensor nonideal properties. As speed increases, the temporal frequency of spatial disturbances increases and the inertia of the machine becomes increasingly effective at damping out the position state oscillations due to these disturbances. This is not the case for position sensor nonideal properties, which are spatial in nature and therefore independent of speed. This distinction between spatial torque disturbances and position sensor nonideal properties indicates

that the best operating conditions, in which to update the MRAS-based decoupling vector are high speed, low load, non-dynamic operating conditions.

D. MRAS Utilization With Low-Resolution Incremental Encoders

As mentioned in the Introduction, the discrete nature of Hall effect-based position measurement and incremental optical encoders can be interpreted as rotating vectors containing significant spatial harmonic content. While the MRAS structure can be used to improve upon these types of sensors by decoupling their most significant position measurement error harmonics, the solutions presented in [2], [12], and [14] are closed form and are recommended over the methods discussed here for applications utilizing low-resolution encoders.

VI. CONCLUSION

This paper has investigated improving the accuracy of low/intermediate quality vector-based position sensors through nonideal sensor property decoupling via MRAS methods. Key conclusions are provided as follows.

- Nonideal sensor properties result in spatially dependent position measurement errors. Sensor-induced errors can be significantly reduced through the decoupling of non-ideal sensor properties using methods well-suited to the self-commissioning and quality testing of sensors.
- An MRAS structure that converges upon nonideal sensor property estimates and decouples these nonideal properties resulting in enhanced sensor accuracy has been proposed, developed, and evaluated. The proposed MRAS methods presented here can be applied to many forms of vector-based position measurement such as the use of magnetoresistive sensors, sine/cosine encoders, resolvers and self-sensing (sensorless) methods.
- Simulation and experimental evaluation of the MRAS-based nonideal sensor property decoupling structure display improved sensor accuracy. Level of improvement will depend on sensor quality and initial calibration. For the results shown in Fig. 10, the peak-to-peak value of the position error was reduced by a factor of approximately 4.5. This is likely an underestimate of the MRAS' capability to improve sensor accuracy given limitations in the experimental test stand and the evaluation method.
- Correlation in the MRAS structure takes place between the MRE and spatially harmonic rotating unit vectors. Since the correlation is spatial in nature, temporal domain phenomenon such as resonance or temporal load harmonics will not deteriorate the capability of the MRAS to estimate and decouple position sensor nonideal spatial properties. This is also true for spatial load properties so long as they do not share spatial harmonic numbers with the rotating unit vector correlation functions.

ACKNOWLEDGMENT

The authors would like to thank the motivation provided by the Wisconsin Electrical Machine and Power Electronic Consortium (WEMPEC) of the University of Wisconsin–Madison and Woodward, Inc.

REFERENCES

- [1] M. W. Degner and R. D. Lorenz, "Using multiple saliencies for the estimation of flux, position, and velocity in AC machines," *IEEE Trans. Ind. Appl.*, vol. 34, no. 5, pp. 1097–1104, Sep./Oct. 1998.
- [2] T. R. Tesch "Dynamic torque estimation in a sensor limited environment," Ph.D. dissertation, Dept. Mech. Eng., Univ. Wisconsin–Madison, Madison, WI, USA, 2005.
- [3] D. C. Hanselman, "Resolver signal requirements for high accuracy resolver-to-digital conversion," *IEEE Trans. Ind. Electron.*, vol. 37, no. 6, pp. 556–561, Dec. 1990.
- [4] T. Shao, Y. Fan, Y. Zhang, S. Zhang, and J. Ma, "Research on error compensation algorithm of magneto-resistive electronic compass," in *Proc. ICEMI*, 2011, vol. 4, pp. 291–293.
- [5] L.-Y. Shi, Q. Hong, and W.-Y. Song, "A research of an improved ellipse method in magneto-resistive sensor error compensation," in *Proc. ICMA*, 2009, pp. 4105–4109.
- [6] R. Hoseinnezhad, A. Bab-Hadiashar, and P. Harding, "Calibration of resolver sensors in electromechanical braking systems: A modified recursive weighted least-squares approach," *IEEE Trans. Ind. Electron.*, vol. 54, no. 2, pp. 1052–1060, Apr. 2007.
- [7] J. Bergas-Jané *et al.*, "High-accuracy all-digital resolver-to-digital conversion," *IEEE Trans. Ind. Electron.*, vol. 59, no. 1, pp. 326–333, Jan. 2012.
- [8] S.-H. Hwang, H.-J. Kim, J.-M. Kim, L. Liu, and H. Li, "Compensation of amplitude imbalance and imperfect quadrature in resolver signals for PMSM drives," *IEEE Trans. Ind. Appl.*, vol. 47, no. 1, pp. 134–143, Jan./Feb. 2011.
- [9] A. Bunte and S. Beineke, "High-performance speed measurement by suppression of systematic resolver and encoder errors," *IEEE Trans. Ind. Electron.*, vol. 51, no. 1, pp. 49–53, Feb. 2004.
- [10] L. Wang and T. Emura, "High-precision interpolation using two-phase type PLL for encoders that have distorted waveforms," in *Proc. IEEE Int. Conf. Intell. Process. Syst.*, Beijing, China, Oct. 1997, pp. 82–87.
- [11] R. D. Lorenz and K. Van Patten, "High resolution velocity estimation for all digital, AC servo drives," *IEEE Trans. Ind. Appl.*, vol. 27, no. 4, pp. 701–705, Jul./Aug. 1991.
- [12] T. R. Tesch and R. D. Lorenz, "Disturbance torque and motion state estimation with low-resolution position interfaces using heterodyning observers," *IEEE Trans. Ind. Appl.*, vol. 44, no. 1, pp. 124–134, Jan./Feb. 2008.
- [13] R. D. Lorenz and D. B. Lawson, "A simplified approach to continuous, on-line tuning of field oriented induction machine drives," *IEEE Trans. Ind. Appl.*, vol. 26, no. 3, pp. 420–425, May/Jun. 1990.
- [14] M. C. Harke, G. D. Donato, F. G. Capponi, T. R. Tesch, and R. D. Lorenz, "Implementation issues and performance evaluation of sinusoidal, surface-mounted pm machine drives with Hall-effect position sensors and a vector-tracking observer," *IEEE Trans. Ind. Appl.*, vol. 26, no. 3, pp. 161–173, Jan./Feb. 2008.
- [15] G. Wang, H. Zhan, G. Zhang, X. Gui, and D. Xu, "Adaptive compensation method of position estimation harmonic error for EMF-based observer in sensorless IPMSM drives," *IEEE Trans. Power Electron.*, vol. 29, no. 6, pp. 3055–3064, Jun. 2008.



Caleb W. Secrest received the B.S and M.S. degrees in mechanical engineering from the University of Wisconsin–Madison, Madison, WI, USA, in 2010 and 2013, respectively, where he is currently working toward the Ph.D. degree with focus on improving motor drive precision in order to utilize it as an embedded application-specific sensor.

In 2011, he joined the Wisconsin Electric Machines and Power Electronics Consortium as a Graduate Researcher under Prof. R. D. Lorenz. His interests include ac machines/drives, power electronics, and

control systems.



Jon S. Pointer received the B.S. and M.S. degrees in mechanical engineering from Colorado State University, Fort Collins, CO, USA, in 1989 and 1996, respectively.

He is a Principal Engineer with Woodward, Inc., Fort Collins, CO, USA, with 25 years experience in the design and analysis of mechanical and electro-mechanical hardware for large, industrial, on-engine applications.

Mr. Pointer is a Licensed Professional Engineer in the State of Colorado.



Michael R. Buehner (S'05–M'10) received the B.S., M.S., and Ph.D. degrees in electrical engineering from Colorado State University, Fort Collins, CO, USA, in 2002, 2004, and 2010, respectively.

He is currently a Control Systems Analyst with Woodward, Inc., Fort Collins, CO, USA, where he focuses on robust controls and prognostics for engine system applications.



Robert D. Lorenz (S'83–M'84–SM'91–LF'98) received the B.S., M.S., and Ph.D. degrees from the University of Wisconsin–Madison, Madison, WI, USA, and the M.B.A. degree from the University of Rochester, Rochester, NY, USA.

Since 1984, he has been a member of the faculty of the University of Wisconsin–Madison, where he is the Mead Witter Foundation Consolidated Papers Professor of Controls Engineering in the Department of Mechanical Engineering. He is Co-Director of the Wisconsin Electric Machines and Power Electronics Consortium (WEMPEC). Prior to joining the university, he worked 12 years in industry, in Rochester, NY, on high-performance drives and synchronized motion control. He has authored over 300 published technical papers and is the holder of 25 patents with eight more pending.

Prof. Lorenz was the IEEE Division II Director for 2005/2006, the IEEE Industry Applications Society (IAS) President for 2001, and a Distinguished Lecturer of the IEEE IAS for 2000/2001. He was the recipient of the 2003 IEEE IAS Outstanding Achievement Award, 2006 EPE-PEMC Outstanding Achievement Award, the 2011 IEEE IAS Distinguished Service Award, the 2014 IEEE Richard H. Kaufman Technical Field Award, and the 2014 EPE Outstanding Achievement Award. He was the recipient of 32 IEEE Prize Paper Awards on power electronics, drives, self-sensing, current regulators, motion control, etc.